

Neutral Stellar Winds Toward the High-Mass Star-Forming Region G176.51+00.20

YINGJIE LI,¹ YE XU,¹ JIN-LONG XU,^{2,3} DEJIAN LIU,^{1,4} JINGJING LI,¹ ZEHAO LIN,^{1,4}
 PENG JIANG,^{2,3} SHUAIBO BIAN,^{1,4} CHAOJIE HAO,^{1,4} AND XIUHUI CHEN⁵

¹*Purple Mountain Observatory, Chinese Academy of Sciences, Nanjing 210008, China*

²*National Astronomical Observatories, Chinese Academy of Sciences, Beijing 100101, China*

³*CAS Key Laboratory of FAST, National Astronomical Observatories, Chinese Academy of Sciences, Beijing 100101, China*

⁴*University of Science and Technology of China, Hefei, Anhui 230026, China*

⁵*College of Mathematics and Physics, Hunan University of Arts and Science, Changde, Hunan 415300, China*

ABSTRACT

We observed the high-mass star-forming region G176.51+00.20 using the Five-hundred-meter Aperture Spherical radio Telescope (FAST) with the 19-beam tracking observational mode. This is a pilot work of searching for neutral stellar winds traced by atomic hydrogen (i.e., H I winds) using the high sensitivity H I line toward high-mass star-forming regions where bipolar molecular outflows have been detected with high sensitivity by Liu et al. H I wind was detected in this work only in Beam 1. We find here that, similar to low-mass star formation, no matter how large the inclination is, the H I wind is likely sufficiently strong to drive a molecular outflow. We also find that the abundance of H I in the H I wind is consistent with that of the H I narrow-line self-absorption (HINSA) in the same beam (i.e., Beam 1). This implies that there is probably an internal relationship between H I winds and HINSA. This result also rein-

forces the assertion that H I winds and detected molecular outflows are associated with each other.

Keywords: ISM: jets and outflows - ISM: Molecules - stars: formation ISM: abundances
ISM: kinematics and dynamics

1. INTRODUCTION

One of the important goals of contemporary astrophysics is to understand star formation (e.g., Tan et al. 2014; Bally 2016). Relative to low-mass star formation, the formation mechanism(s) of high-mass stars remain poorly understood (Shu et al. 1987; McKee & Ostriker 2007; Tan et al. 2014), as too are the driving scenario(s) of massive molecular outflows, an essential phase of early high-mass star formation (Arce et al. 2007).

Early studies, especially in the 1980s and 1990s, attempted to ascertain the driving source and mechanism of molecular outflows, mostly for low-mass stars. Snell et al. (1985) and Strom et al. (1986) found that the mass-loss rate of ionized gas is too low to drive CO lobes, and suggested that the stellar winds which drive the CO lobes are largely comprised of neutral gas. Lizano et al. (1988) carefully compared the neutral stellar wind traced by atomic hydrogen (H I wind hereafter) detected in HH 7–11 and the corresponding CO/HCO⁺ outflows, and found that the H I wind was strong enough to drive the molecular outflows. A similar conclusion was drawn by carefully comparing the H I winds in both HH 7–11 and L1551 with the corresponding molecular outflows (see Giovanardi et al. 1992). In such studies, which were performed with the 305 m radio telescope of the Arecibo Observatory, the root mean square (rms) noise was typically $\sim 3.5\text{--}8.5$ mK @ 3.9 km s⁻¹ with beam size of $3'.2\text{--}3'.5$. A model based on the detected H I wind in HH 7–11 was developed by Lizano et al. (1988) to explain the entrainment of ambient molecular gas (i.e., driving the molecular outflow) by the neutral wind. These studies suggested that H I winds are a promising driving source of molecular outflows. However, is such an assertion also true for massive stars?

To answer this question, samples of the molecular outflows have been assembled. For example, ¹²CO, ¹³CO, HCO⁺, and CS outflowing gases have been recently detected with high sensitivity (with

main beam rms noise of dozens of mK) toward nine high-mass star-forming regions using the 13.7 m millimeter telescope of the Purple Mountain Observatory in Delingha (see more details in Liu et al. 2021). Accordingly, an rms noise of ~ 3 mK @ 1.0 km s^{-1} can be achieved with about six hour integrations and a beam size of $\sim 2'.9$ by using the powerful 21 cm H I line detected by the most sensitive ground-based, single-dish Five-hundred-meter Aperture Spherical radio Telescope¹(FAST; Nan 2006; Nan et al. 2011; Jiang et al. 2020). The use of FAST will enabled us to conduct broad investigations of stellar winds toward star-forming regions where molecular outflows have been detected. As such, we have carried out a pilot survey of the H I wind toward detected molecular outflows with highly sensitive observations. The selected object in this work is one of the nine high-mass star-forming regions in Liu et al. (2021), G176.51+00.20.

G176.51+00.20, also known as AFGL 5157 and IRAS 05345+3157, is located 1.8 kpc from Earth (Moffat et al. 1979; Snell et al. 1988). It is a complex region containing multi-generational star formation (e.g., Chen et al. 2003; Dewangan 2019). The main research object in this work is a high-mass star-forming region at a relatively young phase, where H₂O masers and an H II region have been detected (Torrelles et al. 1992a). This region is marked as an ‘‘H II region’’ in figure 1(a) in Dewangan (2019). There is a dense NH₃ core in the center of this region, which has become synonymous with this region (e.g., Torrelles et al. 1992a; Chen et al. 2003; Jiang et al. 2013). By constructing a 3.6 cm map with the Very Large Array, the excitation source of this region was identified as a zero-age main-sequence B3 star (Torrelles et al. 1992b). The bolometric luminosity of this excitation source was determined as $1.7 \times 10^3 L_{\odot}$ via an 8–1200 μm SED fit (see Molinari et al. 2008). The age of this star-forming region was suggested to be $\sim 2 \times 10^5$ yr by investigating the near-infrared H₂ line emission using the 1.88 m telescope of Okayama Astronomical Observatory, Japan (see Chen et al. 2003).

The famous bipolar outflow (traced by ¹²CO) detected by Snell et al. (1988) is centered on the dense NH₃ core (Molinari et al. 2002; Zhang et al. 2005; Dewangan 2019), suggesting that the excitation

¹ <https://fast.bao.ac.cn/>

source of this bipolar outflow is probably the zero-age main-sequence B3 star (see [Torrelles et al. 1992b](#)). [Liu et al. \(2021\)](#) confirmed this bipolar outflow with high-sensitivity ^{12}CO , ^{13}CO , C^{18}O , HCO^+ , and CS line emission observations, and broadened the blue lobe of this outflow (traced by ^{12}CO) by a factor of ~ 2 . This makes the dense NH_3 core more suitable to investigate whether its H I wind is strong enough to drive the molecular outflows.

The remainder of this paper is organized as follows. In Section 2, we describe the data used in this work. Section 3 analyses the H I wind associated with the molecular outflows. In Section 4, discussion of whether the H I wind is strong enough to drive the molecular outflows is presented. Finally, Section 5 gives a summary and the main conclusions of this work.

2. H I OBSERVATIONS WITH FAST

FAST is located in Guizhou Province of southwest China ([Nan et al. 2011](#)). It is equipped with a 19-beam receiver (the frequency range is 1.0–1.5 GHz with a bandwidth of 500 MHz) and has dual linear polarizations (i.e., XX and YY; see [Li et al. 2018](#); [Jiang et al. 2019, 2020](#)). The spectral resolution is ~ 477 Hz, corresponding to a velocity resolution of ~ 0.1 km s $^{-1}$ at 1.4 GHz. The half-power beam width (HPBW) is $\sim 2.9'$ at 1.4 GHz, and the pointing error is $\sim 0.2'$ (see [Jiang et al. 2019, 2020](#)).

Observations toward G176.51+00.20 were conducted on August 19th and 20th, 2021. The observational mode was 19-beam tracking, and the total integration time was 335 minutes with a sampling rate of one second. A new algorithm is used to obtain a flat baseline. In this algorithm, there are three main steps: (1) a polynomial fitting over the velocity range of $[-7000, 7000]$ km s $^{-1}$; (2) removing the standing waves by using fast Fourier transforms; (3) calibrating the unsmooth parts in the baseline by extreme envelope curves (for more details of the pipeline used to obtain the flat baseline, see [Liu et al. 2022](#)). For Beams 2, 3, 5, 6, and 8–19, the spectra of two linear polarizations (i.e., XX and YY) were dealt with separately and then averaged. However, because of the bad baseline, only the YY polarization spectrum from Beam 1 and the XX spectra from Beams 4 and 7 were retained. The mean rms noise of the nineteen spectra is ~ 7 mK @ 0.1 km s $^{-1}$ (see the rms noise of each spectrum in Table 1). Figure 1 presents the positions of the central seven beams superposed on CO

Table 1. List of the Positions and Rms Noise of the Nineteen Beams

Index	R.A.	Decl.	Rms	Index	R.A.	Decl.	Rms
	(J2000)	(J2000)	(mK)		(J2000)	(J2000)	(mK)
1	05 ^h 37 ^m 53 ^s	31°59′58″	8.0	2	05 ^h 38 ^m 20 ^s	32°00′00″	6.1
3	05 ^h 38 ^m 07 ^s	31°55′01″	6.8	4	05 ^h 37 ^m 39 ^s	31°54′59″	11.2
5	05 ^h 37 ^m 26 ^s	31°59′57″	6.1	6	05 ^h 37 ^m 39 ^s	32°04′56″	6.2
7	05 ^h 38 ^m 06 ^s	32°04′57″	7.7	8	05 ^h 38 ^m 47 ^s	32°00′01″	8.8
9	05 ^h 38 ^m 34 ^s	31°55′02″	6.5	10	05 ^h 38 ^m 20 ^s	31°50′03″	7.7
11	05 ^h 37 ^m 53 ^s	31°50′02″	6.3	12	05 ^h 37 ^m 26 ^s	31°50′00″	5.9
13	05 ^h 37 ^m 12 ^s	31°54′58″	6.6	14	05 ^h 36 ^m 59 ^s	31°59′55″	6.9
15	05 ^h 37 ^m 12 ^s	32°04′54″	6.3	16	05 ^h 37 ^m 26 ^s	32°09′53″	6.9
17	05 ^h 37 ^m 53 ^s	32°09′55″	6.1	18	05 ^h 38 ^m 20 ^s	32°09′56″	6.9
19	05 ^h 38 ^m 33 ^s	32°04′58″	6.7				

molecular maps, and Figure 2 shows the spectrum of the central seven beams and the H I narrow-line self-absorption lines (HINSA, T_{ab}) in each beam (see Li et al. 2022).

3. DATA ANALYSIS AND RESULTS

3.1. Identification of the H I Wind

We defined the excess brightness temperature (EBT, hereafter) as the spectrum resulting from the subtraction of the average spectrum of the off-positions from the spectrum of the on-position (i.e., the target beam). Similar to the work of Lizano et al. (1988), the six beams located immediately around the target beam (i.e., which acted as the on-position) were used as the off-positions. The baseline of the EBT was flat, i.e., the rms noise was $\sim 1.8\text{--}2.3$ mK @ 2.0 km s⁻¹ (i.e., smooth over twenty channels), except for Beams 3 and 4, whose rms noises were, respectively, 3.3 and 6.1 mK @ 2.0 km s⁻¹. We also defined the standard deviation (STD) of EBT (SEBT) to evaluate the variation among the spectrum from different off-positions. For instance, for Beam 1, we first separately calculated the EBT of Beam 1 relative to its six surrounding beams, and then computed the STD of these six EBTs, which is the SEBT of Beam 1.

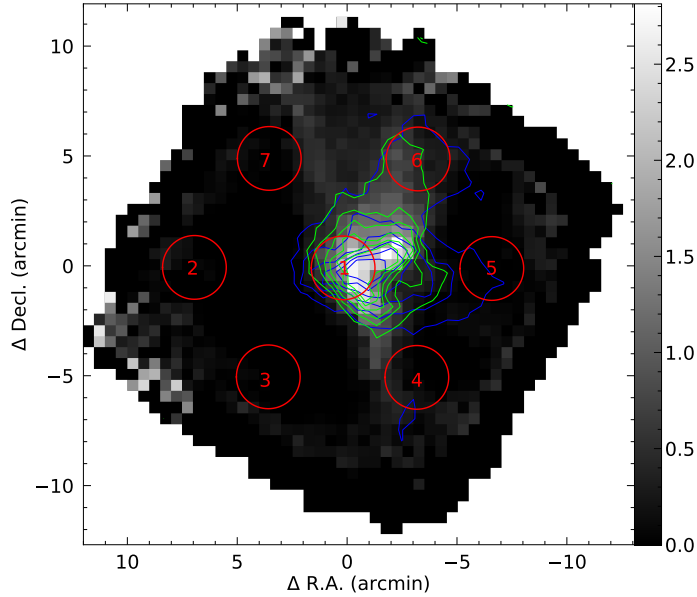


Figure 1. The central seven beams superposed on the integrated intensity map of C^{18}O in the range of $[-30, -10]$ km s^{-1} with the molecular data from Liu et al. (2021). The blue and lime contours show the integrated intensity map of ^{12}CO and ^{13}CO in the same velocity range as the C^{18}O map.

3.1.1. $H\text{ I}$ Wind in Beam 1

From Figure 3, it can be seen that Beam 1 presents an evident high-velocity red wing whose maximum velocity exceeds ~ 120 km s^{-1} . The SEBT is also small in the high-velocity red wing, indicating this wing may well be true, rather than the changes or fluctuations of the emission from one beam area to another. This high-velocity red wing was crudely fitted by a “triangular fit” (see e.g., Lizano et al. 1988). Assuming this high-velocity line wing is bipolar, the symmetric line of the high-velocity red wing with respect to the line center, $v_{c,w}$, is also presented as a red oblique line (see the red isosceles triangle of the high-velocity bipolar wing in Figure 3(a)). Therein, $v_{c,w}$ is taken as the velocity of the corresponding HINSA (see Figure 2 and Li et al. 2022), which is indicated as a red vertical line in Figure 3(a). This symmetric line is referred to as the presumed high-velocity blue wing, although there is no blue wing present in Figure 3(a). However, we find that the velocity of the bulge in Beam 7 (see Figure 3(g)) overlaps with that of the presumed high-velocity blue wing in Beam 1. Therefore, a further analysis of the high-velocity line wing in Beam 1 was conducted where we took different beams as the off-positions (see Figure 4).

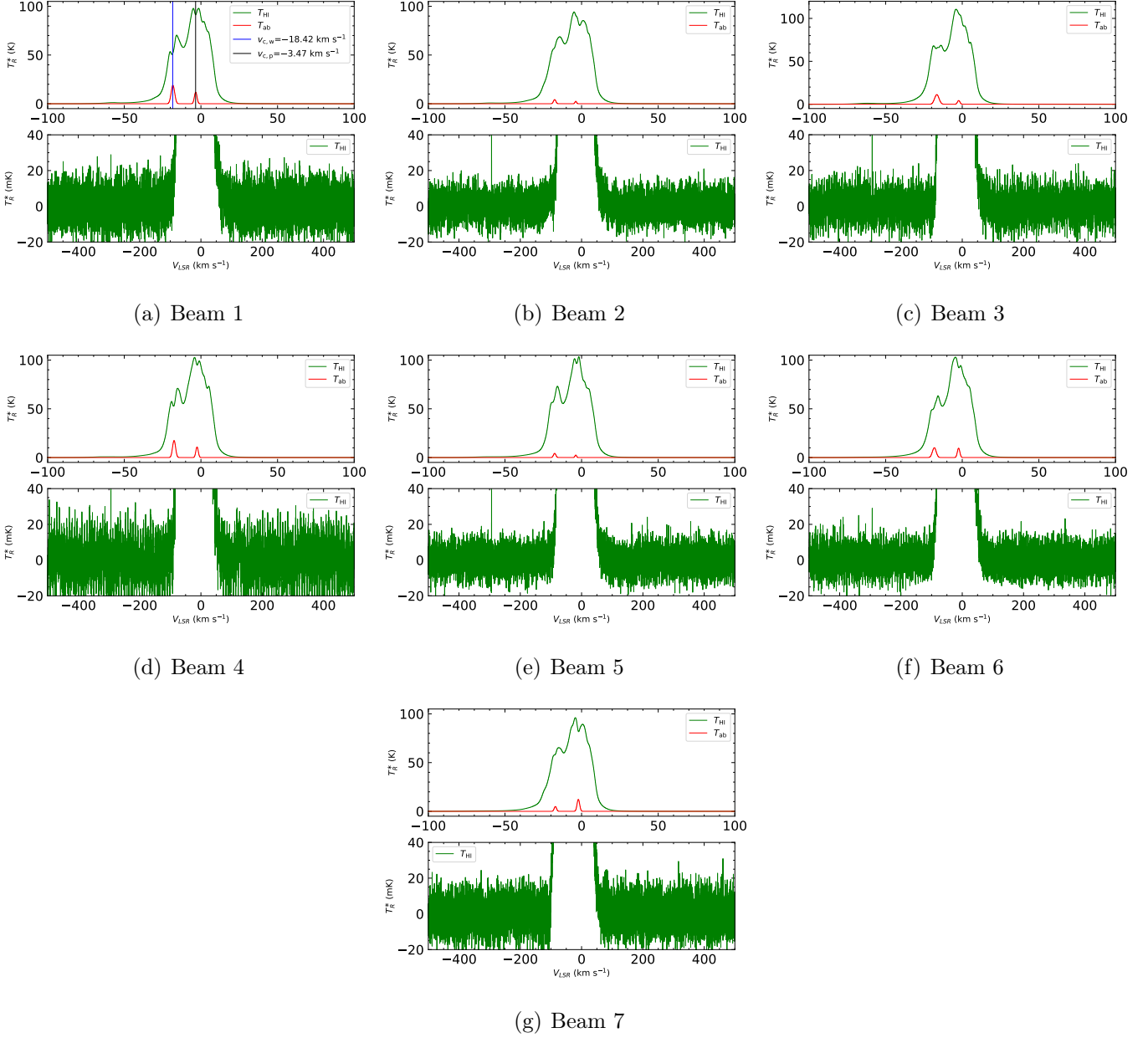


Figure 2. Top: spectra of the central seven beams (green lines) and the HINSA (T_{ab} , red lines) obtained in Li et al. (2022). Bottom: the flat baseline. $v_{c,w}$ represents the central velocity of the HINSA feature (i.e., at -18.42 km s^{-1}) associated with the H I wind (see below), and $v_{c,p}$ represents the central velocity of another HINSA feature (i.e., at -3.47 km s^{-1}) in Beam 1.

When using Beams 2–7 as off-positions (see Figures 3), we also took beams orientated along West–East (i.e., Beams 2 and 5), Northeast–Southwest (i.e., Beams 3 and 6), Northwest–Southeast (i.e., Beams 4 and 7), and also using Beams 2–6 as off-positions (see Figures 4(a)–(d), respectively). These

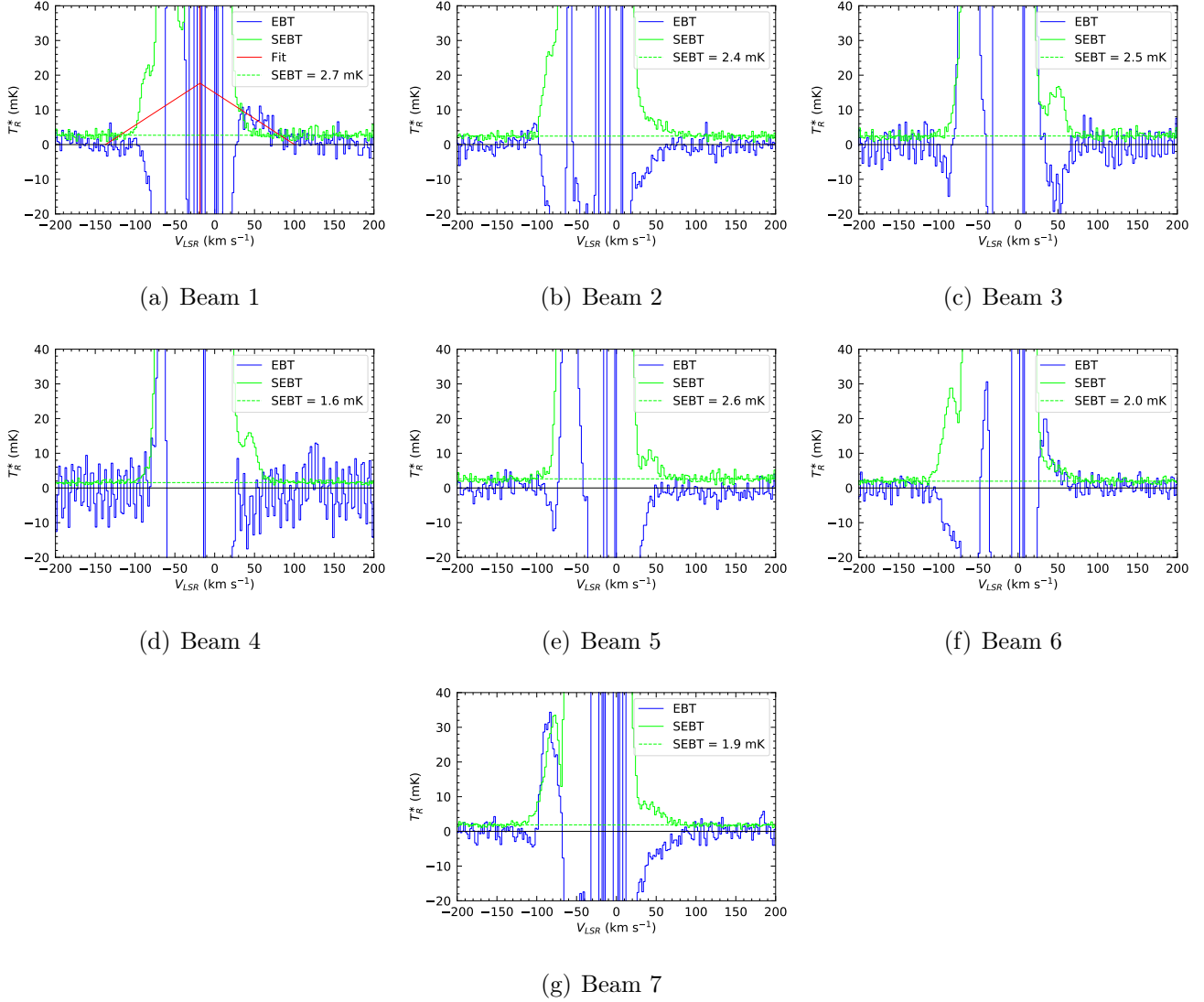


Figure 3. EBT (blue lines) and SEBT (green lines) of Beams 1–7 (smoothed over twenty channels, blue lines). For the spectrum in which the high-velocity line wing was present, the “triangular fit” is plotted as a red oblique line, where the line center (red vertical line) is taken as the velocity of the HINSA (see Figure 2 and Li et al. 2022).

five cases are referred to as Normal, W–E, NE–SW, NW–SE, and Lack Beam 7. The high-velocity red wing remains basically unchanged no matter which beams are used as off-positions (see Figure 4 and quantitative comparison in Section 3.2), and the high-velocity blue wing is also present as long as the off-positions do not contain Beam 7. Therefore, Beam 1 probably presents a high-velocity bipolar wing, but the high-velocity blue wing is contaminated by other components. In addition, there is a small pit between the “triangular fit” of the EBT for the cases of W–E, NE–SW, and NW–SE (see

the left green oblique line in Figures 4(a)–(c)) and the presumed high velocity blue wing (see red oblique line). This small pit likely causes the green oblique line to deviate from the red oblique line, which implies that this high-velocity bipolar wing is probably symmetrical; therefore, we identify it as a bipolar H I wind. Because the blue lobe is contaminated by other components, and we presume that this H I wind is a symmetrical bipolar H I wind, we applied the fitting result of the red lobe to the blue lobe.

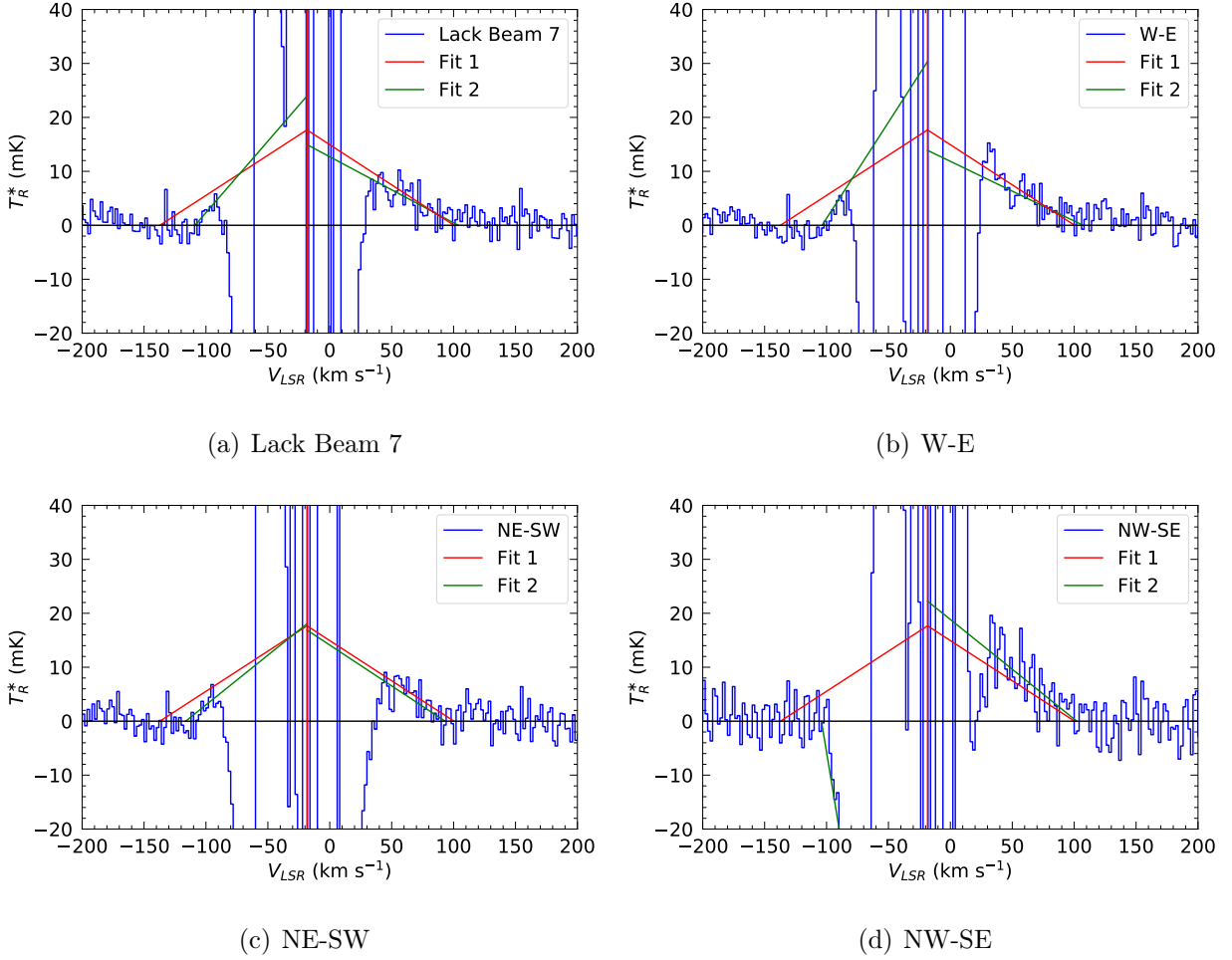


Figure 4. EBT obtained from using different beams as off-positions. The red lines (“Fit 1”) are the same as that in Figure 3(a). The green lines (“Fit 2”) are the results of the “triangular fit” of the EBTs (fit separately for the blue and red lobes). Lack Beam 7: using Beams 2–6 as off-positions; W–E: taking Beams 2 and 5 as off-positions; NE–SW: using Beams 3 and 6 as off-positions; NW–SE: using Beams 4 and 7 as off-positions.

3.1.2. The EBT in Other Beams

Table 2. Comparison of the Physical Parameters Determined with Different Off-positions

Classification	$M_{\text{HI,wind}}$ (M_{\odot})	$P_{\text{HI,wind}}$ ($M_{\odot} \text{ km s}^{-1}$)	$V_{\text{max,wind}}$ (km s^{-1})	$V_{\text{mean,wind}}$ (km s^{-1})
Normal	0.11 ± 0.02	4.03 ± 1.76	120.6 ± 16.3	40.2 ± 5.4
Lack Beam 7	0.10 ± 0.02	3.48 ± 2.22	124.7 ± 20.7	41.6 ± 6.9
W-E	0.09 ± 0.02	3.16 ± 3.56	129.7 ± 25.7	42.2 ± 8.6
NE-SW	0.10 ± 0.02	3.33 ± 1.65	112.6 ± 16.2	37.5 ± 5.4
NW-SE	0.14 ± 0.02	5.20 ± 2.26	122.2 ± 16.0	40.7 ± 5.3

The bulge in the blue line wing of Beam 2 is, in fact, present in only one polarization spectrum (i.e., YY). Therefore, this blue line wing is highly likely a fake high-velocity line wing. Figure 3 also presents other high-velocity features, e.g., wings with negative intensities in right side of EBTs in Beams 2 and 7, and wings with positive intensities in right side of EBTs in Beam 6, etc. These high-velocity features are more likely to stem from the changes or fluctuations of the emission from one beam area to another, because these features are located where SEBTs are large.

3.2. Physical Parameters of the H I Wind

We calculated the mass, $M_{\text{HI,wind}}$, momentum, $P_{\text{HI,wind}}$, maximum velocity, $V_{\text{max,wind}}$, and average velocity, $V_{\text{mean,wind}}$, of the red lobe of the H I wind (“triangular fit”) corresponding to different off-positions, i.e., the case of Normal (see red line in Figure 3(a)), Lack Beam 7, W–E, NE–SW, and NW–SE (see green lines in Figures 4(a)–(d)). The specific calculations without inclination correction are presented in Section A. The results show that all the values of $M_{\text{HI,wind}}$, $P_{\text{HI,wind}}$, $V_{\text{max,wind}}$, and $V_{\text{mean,wind}}$ are consistent with each other within the errors (all the errors presented in this work are 1σ uncertainties) for all the five cases (see the physical values in Table 2). This reinforces the conclusion that the red lobe of the H I wind is real, and the case of Normal can reflect the physical properties of the red lobe of the H I wind. Therefore, the calculations below are based on the case of Normal.

The “triangular fit” of the red lobe of the H I wind produced $T_{\text{wind}}(v) = (14.94 \pm 1.32) + (-0.15 \pm 0.02) \cdot v$. The maximum velocity, $V_{\text{max,wind}}$, and the average velocity, $V_{\text{mean,wind}}$, without inclination

correction are, respectively, 120.6 ± 16.3 and 40.2 ± 5.4 km s⁻¹, where $V_{\text{mean,wind}} = V_{\text{max,wind}}/3$ for the triangular profile. $V_{\text{max,wind}}$ (and also $V_{\text{mean,wind}}$) are 0.7 and 0.8 times that in HH 7–11 and in L1551 (both are located in low-mass star-forming regions; see [Lizano et al. 1988](#); [Giovanardi et al. 1992](#)), respectively. The column density of the red lobe of the H I wind, $N_{\text{HI,wind}}$, is $(1.94 \pm 0.30) \times 10^{18}$ cm⁻² (see [Table 3](#)). Assuming that the H I wind occupies the same spatial location as the molecular outflows, and both of them are angularly unresolved (e.g., [Lizano et al. 1988](#)), $N_{\text{HI,wind}}$ is two orders of magnitude smaller than the column density of the outflow traced by ¹²CO, and three orders of magnitude smaller than that traced by ¹³CO, HCO⁺, and CS (see the column density of the molecular outflows in [Liu et al. 2021](#)).

¹³CO is proved to be a great tracer of the molecular column density, and the fractional HINSA abundance (where the molecular column density is traced by ¹³CO) is $\sim 1.1 \times 10^{-3}$ ([Li et al. 2022](#)). We also calculated the abundance of H I in the H I wind, $X_{\text{HI,wind}}$, as:

$$X_{\text{HI,wind}} = \frac{N_{\text{HI,wind}}}{N_{\text{HI,wind}} + 2N_{\text{H}_2,\text{outflow}}}, \quad (1)$$

where $N_{\text{H}_2,\text{outflow}}$ is the column density of the molecular outflow (that is traced by ¹²CO, ¹³CO, HCO⁺, or CS; see [Liu et al. 2021](#)). The results of $X_{\text{HI,wind}}$ are listed in [Table 3](#). $X_{\text{HI,wind}}$, determined by the molecular outflow traced by ¹³CO, is $\sim 1.0 \times 10^{-3}$ (only for the red lobe), which is consistent with the fractional HINSA abundance.

This consistency reveals an internal correlation between the H I wind and HINSA. It also supports the conclusion of the mixture of the H I wind and the molecular outflow because HINSA is probably mixed with the gas in the cold, well-shielded regions of the molecular clouds (see [Li & Goldsmith 2003](#); [Li et al. 2022](#)). However, observations with higher resolution are required to confirm the correlation between the H I wind and HINSA, and a larger sample is essential to rule out that the observed consistency here is only a coincidence.

We also calculated the mass, $M_{\text{HI,wind}}$, momentum, $P_{\text{HI,wind}}$, and kinetic energy, $E_{\text{HI,wind}}$, of the H I wind (combine the values of the two lobes) without inclination correction (see the calculations in [Section A](#) and the values in [Table 3](#)). The mass and momentum over the overall flow history are

Table 3. Physical Properties of the H I Wind without Inclination Correction

Quantity	Value (1σ uncertainty)	Noting
$N_{\text{HI,wind}}$ (cm^{-2})	$(1.94 \pm 0.30) \times 10^{18}$	See Equation (A2)
$X_{\text{HI,wind}}$	$\sim (4.6, 1.0, 0.4, 0.8) \times 10^{-3}$	For ^{12}CO , ^{13}CO , HCO^+ and CS , See Equation (1)
$M_{\text{HI,wind}}$ (M_{\odot})	0.22 ± 0.03	Combined two lobes, see Equation (A4)
$P_{\text{HI,wind}}$ ($M_{\odot} \text{ km s}^{-1}$)	8.05 ± 3.52	Combined two lobes, see Equation (A5)
$V_{\text{max,wind}}$ (km s^{-1})	120.6 ± 16.3	See Equation (A3)
$V_{\text{mean,wind}}$ (km s^{-1})	40.2 ± 5.4	$V_{\text{max,wind}}/3$
$E_{\text{HI,wind}}$ (erg)	$(3.4 \pm 1.5) \times 10^{46}$	See Equation (A7)
$\Delta M_{*,\text{m}}$ (M_{\odot})	$\sim 0.43, \sim 0.61, \sim 3.68, \sim 1.53$	For ^{12}CO , ^{13}CO , HCO^+ and CS
$\Delta M_{*,\text{ame}}$ (M_{\odot})	1.3, -5.8 , 10.5, 6.5, 9.0, 2.7	Respectively relative to Beams 2–7
$l_{\text{HI,wind}}$ (pc)	0.8	See l_{outflow} in Liu et al. (2021)
t_{a} (yr)	$(1.9 \pm 0.2) \times 10^4$	$l_{\text{HI,wind}}/V_{\text{mean,wind}}$
\dot{M}_{a} ($M_{\odot} \text{ yr}^{-1}$)	$(12.2 \pm 3.6) \times 10^{-6}$	$M_{\text{HI,wind}}/t_{\text{a}}$
t (yr)	$(5.3 \pm 3.5) \times 10^5$	$\Delta M_{*,\text{a}}/\dot{M}_{\text{a}}$
$L_{\text{HI,wind}}$ (L_{\odot})	16.0 ± 10.1	$\frac{1}{2}\dot{M}_{\text{a}}V_{\text{max,wind}}^2$

larger than the values estimated above (see Lizano et al. 1988). The values of $M_{\text{HI,wind}}$, $P_{\text{HI,wind}}$, and $E_{\text{HI,wind}}$ are larger than that in HH 7–11 (see Lizano et al. 1988; Giovanardi et al. 1992) by a factor of ~ 7 , ~ 5 , and ~ 4 , respectively, and larger than that in L1551 (see Giovanardi et al. 1992) by a factor of ~ 26 , ~ 20 , and ~ 6 , respectively.

4. DISCUSSION

4.1. Dynamical Comparison Between the H I Wind and the Molecular Outflow

To determine whether the H I wind is strong enough to drive the molecular outflow, analyses of two dimensions were conducted and are presented here; i.e., the mass loss of the excitation star and the lifetime of the H I wind.

4.1.1. Mass Loss of the Excitation Star

If we assume that the molecular outflow is entrained by the H I wind originally ejected from the star, then the mass loss, $\Delta M_{*,m}$, from the excitation star over the entire history of mass loss is $M_{*,m} = P_{m,outflow}/V_{max,wind}$ (see [Lizano et al. 1988](#)), where $P_{m,outflow}$ is the momentum of the molecular outflow (see [Liu et al. 2021](#)). Both the blue and red lobes of the molecular outflow are included in the calculation. The total $\Delta M_{*,m}$, which combines contributions from the ^{12}CO , ^{13}CO , HCO^+ , and CS outflows, is $6.26 \pm 0.80 M_{\odot}$ (see the contribution from each molecular outflow in [Table 3](#)). Because [Liu et al. \(2021\)](#) did not give the error of $P_{m,outflow}$, the error of $\Delta M_{*,m}$ is only from $V_{max,wind}$ and no error is presented in [Table 3](#). It is worth noting that the total $\Delta M_{*,m}$ is probably overestimated because the values of $P_{m,outflow}$ are corrected for the abundance of the corresponding tracer (see [Liu et al. 2021](#)).

Similar to the work in [Lizano et al. \(1988\)](#), we calculated the atomic mass excesses, $\Delta M_{*,ame}$, of the line core of Beam 1 relative to the line core of the six beams tightly around Beam 1, assuming that the low-velocity material is associated with the source and fills the beams of FAST. We tested different velocity spans, v_s , as line core (see [Figure 5](#)), where $v_s = v_{c,w} - v$ and only $v < v_{c,w}$ is considered because there is a strong component at $\sim -3.5 \text{ km s}^{-1}$. The increase of $\Delta M_{*,ame}$ at $v_s \sim 30\text{--}45 \text{ km s}^{-1}$ may be the results of the influence of the component at $\sim -57 \text{ km s}^{-1}$ (see [Figure 2](#)). $\Delta M_{*,m}$ is flat at $v_s \sim 15\text{--}23 \text{ km s}^{-1}$, indicating that the influence of the component at $\sim -3.5 \text{ km s}^{-1}$ may be small. We set the velocity range of $v_{c,w} - v \leq 20 \text{ km s}^{-1}$ as the line core, corresponding to $v_s \sim 20 \text{ km s}^{-1}$ (i.e., at the middle of the flat region). The atomic mass excesses of Beams 1 to its surrounding beams are systematically positive (except for those between Beams 1 and 3). In addition, such systematically positive of the atomic mass excesses is invalid for the case of Beams 2 and 4–7 relative to their surrounding beams. ²These facts indicate that atomic gas flows out from

² For Beams 2 and 4–7, the mass excess relative to their six surrounding beams is not systematically positive. For instance, the atomic mass excesses of Beam 2 relative to its six surrounding beams are, respectively, -0.4 , -4.6 , -3.2 , -2.3 , 3.2 , and $0.6 M_{\odot}$ (starting from the West beam and counting counterclockwise); and for Beam 5, the corresponding values are -2.7 , 0.7 , 1.8 , -3.6 , 0.8 , and $-4.9 M_{\odot}$. For Beam 3, the corresponding values are 10.9 , 0.4 , -0.9 , 2.3 , 5.2 , and $4.4 M_{\odot}$.

Beam 1, and these atomic mass excesses may be an indicator of accumulated atomic mass loss from the excitation star, $\Delta M_{*,a}$ (e.g., Lizano et al. 1988).

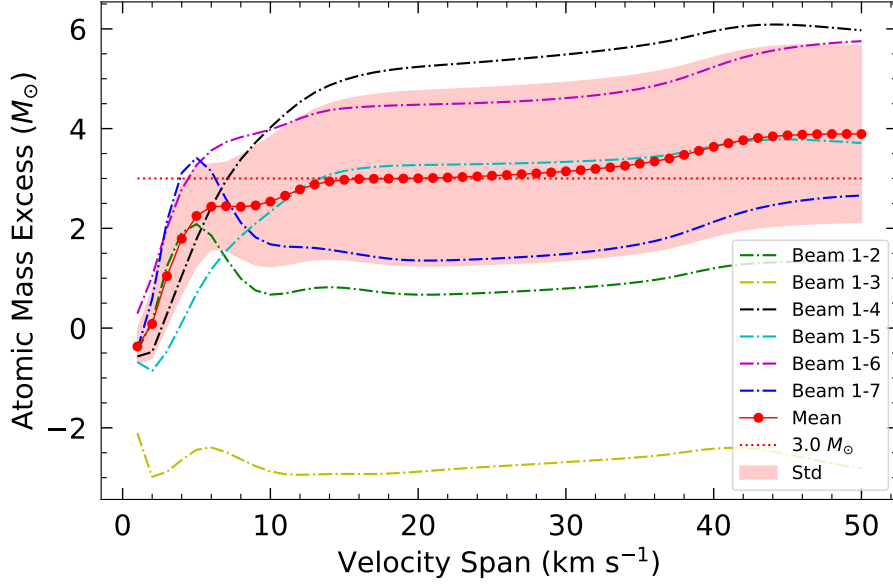


Figure 5. Atomic mass excesses, $\Delta M_{*,ame}$, as a function of velocity spans, v_s . “Beam 1- i ” represent the atomic mass excess of Beam 1 relative to Beam i , “Mean” and “Std” present the mean and STD values of the five atomic mass excesses (i.e., except for that between Beams 1 and 3), and the red dashed line that labeled as “ $3.0 M_\odot$ ” indicates $\Delta M_{*,ame} = 3.0 M_\odot$.

The atomic mass excesses of Beam 1 relative to its surrounding beams with a velocity range of $|v_{c,w} - v| \leq 20 \text{ km s}^{-1}$ are listed in Table 3, which are set to be two times of the corresponding atomic mass excesses with a velocity range of $v_{c,w} - v \leq 20 \text{ km s}^{-1}$. The average value of $\Delta M_{*,ame}$ over the five atomic mass excesses (i.e., except for that between Beams 1 and 3, where the atomic mass excesses are significantly different from the other atomic mass excesses) is $6.0 \pm 3.5 M_\odot$ (i.e., $\Delta M_{*,a} \sim 6.0 \pm 3.5 M_\odot$), where $3.5 M_\odot$ is the STD of the five atomic mass excesses. The error of atomic mass excess inherited from the original spectrum is far less than $3.5 M_\odot$, and therefore no error of atomic mass excess is presented in Table 3. $\Delta M_{*,a} \sim \Delta M_{*,m}$, and the outflowing atomic gas would undergo deceleration when it entrained molecular outflow gas, indicating that the velocity associated with $\Delta M_{*,a}$ may be not less than that associated with $\Delta M_{*,m}$ and H I wind is likely strong enough to drive the molecular outflow.

4.1.2. *Lifetime of the H I Wind*

The lifetime of the H I wind flow, i.e., the total duration of the flow, t , without inclination correction was estimated according to [Lizano et al. \(1988\)](#). The distance from the H I wind to the central excitation star, $l_{\text{HI,wind}}$, was set as the outflow length, l_{outflow} , of the molecular outflow (which, here, corresponds to the red lobe of ^{12}CO ; see [Liu et al. 2021](#)), i.e., $l_{\text{HI,wind}} \sim 0.8$ pc. The crossing time of the H I wind, t_a , is then $t_a = l_{\text{HI,wind}}/V_{\text{mean,wind}} = (1.9 \pm 0.2) \times 10^4$ yr, where the uncertainty comes only from $V_{\text{mean,wind}}$ because no error of l_{outflow} was given by [Liu et al. \(2021\)](#). Therefore, the stellar mass-loss rate, \dot{M}_a , is $\dot{M}_a = M_{\text{HI,wind}}/t_a = (12.2 \pm 3.6) \times 10^{-6} M_{\odot} \text{ yr}^{-1}$. This value (without inclination correction) is larger than that in HH 7–11 by a factor of ~ 2 and larger than that in L1551 by a factor of ~ 10 (see [Lizano et al. 1988](#); [Giovanardi et al. 1992](#)). The lifetime of the H I wind is $t = \Delta M_{*,a}/\dot{M}_a = (5.3 \pm 3.5) \times 10^5$ yr, where the accumulated atomic mass, $\Delta M_{*,a}$, is set to $6.0 \pm 3.5 M_{\odot}$ (see above). All the physical properties above are listed in Table 3. The dynamical timescale of the red lobe of the molecular outflow, t_{outflow} , as an indicator of the age of the flow, ranges from $1\text{--}5 \times 10^4$ yr traced by four species (i.e., ^{12}CO , ^{13}CO , HCO^+ and CS ; see [Liu et al. 2021](#)). t is about one order of magnitude larger than t_{outflow} , indicating that the H I wind is likely strong enough to drive the molecular outflow. Observations with higher spatial resolution of both H I and molecules are required to further confirm this conclusion.

To further investigate the influence of the inclination, Figure 6 presents both t and t_{outflow} (including those for the ^{12}CO , ^{13}CO , HCO^+ , and CS outflows) under different inclinations. It can be seen that the lifetime of the H I wind is much larger than the timescale of the outflow traced by all the four molecules, no matter what inclination is considered. This suggests that the inclination does not change the inequality of $t \gg t_{\text{outflow}}$.

Moreover, [Chen et al. \(2003\)](#) derived the timescale of the star formation corresponding to this H I wind or molecular outflow as $\sim 2 \times 10^5$ yr by researching the H_2 knots surrounding the excitation source. The inclination of this H I wind or molecular outflow, θ_0 , may be $\sim 69^{\circ} {}^{+8^{\circ}}_{-28^{\circ}}$, assuming that the lifetime of the H I wind equals the timescale of star formation, i.e., $t \sim 2 \times 10^5$ yr.

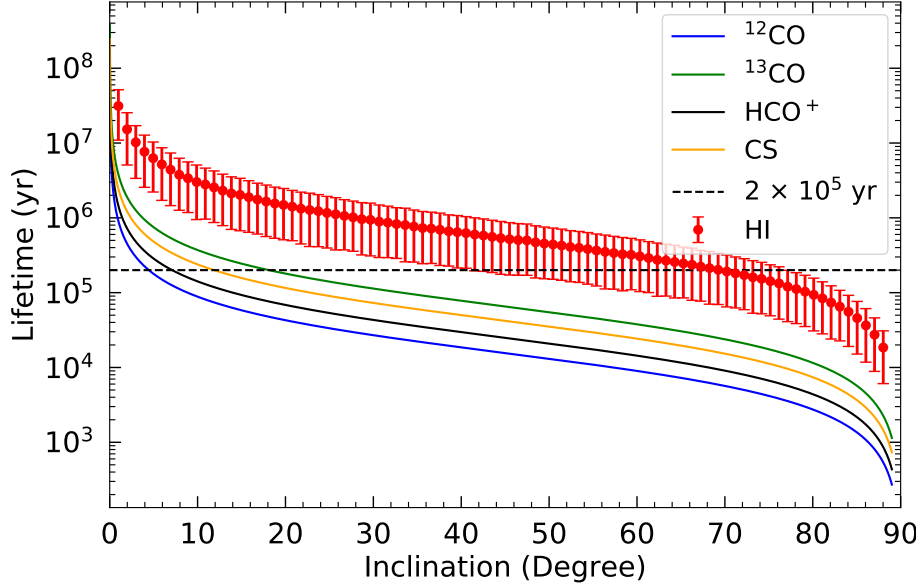


Figure 6. t (red points, where the error bars indicate the 1σ uncertainty) and t_{outflow} (blue solid line for ^{12}CO , green for ^{13}CO , black for HCO^+ , and yellow for CS) as functions of the inclination. The dashed line is the dynamical timescale of the corresponding star formation (i.e., $\sim 2 \times 10^5$ yr; see [Chen et al. 2003](#)).

4.2. Physical Properties with an Inclination of 69°

We next calculated the physical properties of the H I wind assuming that an inclination of 69° (see Table 4). The maximum velocity of the H I wind changes to $\sim 336.2 \pm 44.6$ km s $^{-1}$. This value is larger than that for HH 7–11 (assuming an inclination of 22° ; see [Herbig & Jones 1983](#); [Lizano et al. 1988](#)) by a factor of ~ 2 , and is $\sim 60\%$ of that for L1551 (assuming an inclination of 75° ; see [Snell & Schloerb 1985](#); [Giovanardi et al. 1992](#)). The value of the momentum of the H I wind after inclination correction is $22.66 M_\odot$ km s $^{-1}$, which is larger than that in HH 7–11 by a factor of ~ 12 (see [Lizano et al. 1988](#); [Giovanardi et al. 1992](#)), and a factor of ~ 15 for that in L1551 (see [Giovanardi et al. 1992](#)). The values of the wind’s kinetic energy, i.e., $\sim 2.6 \times 10^{47}$ erg, and the stellar mass-loss rate, i.e., $\sim 3.2 \times 10^{-5} M_\odot$ yr $^{-1}$, are larger than those in HH 7–11 by factors of ~ 28 and ~ 10 , and larger than those in L1551 by factors of ~ 3 and ~ 7 , respectively (see these values in HH 7–11 and L1551 in [Lizano et al. 1988](#); [Giovanardi et al. 1992](#)).

The kinetic luminosity of the H I wind, $L_{\text{HI,wind}} = \frac{1}{2} \dot{M}_a V_{\text{max,wind}}^2$, is $16.0 \pm 10.1 L_\odot$ without inclination correction, which is much less than the bolometric luminosity, L_* , of the excitation source (i.e.,

Table 4. Physical Properties of the H I Wind for an Inclination of 69°

Quantity	Value (1σ uncertainty)
$P_{\text{HI,wind}}$ ($M_\odot \text{ km s}^{-1}$)	22.66 ± 9.63
$V_{\text{max,wind}}$ (km s^{-1})	336.2 ± 44.6
$V_{\text{mean,wind}}$ (km s^{-1})	112.1 ± 14.9
$E_{\text{HI,wind}}$ (erg)	$(2.6 \pm 1.2) \times 10^{47}$
t_{a} (yr)	$(7.2 \pm 0.9) \times 10^3$
\dot{M}_{a} ($M_\odot \text{ yr}^{-1}$)	$(3.2 \pm 0.9) \times 10^{-5}$
t (yr)	$(2.0 \pm 1.4) \times 10^5$
$L_{\text{HI,wind}}$ (L_\odot)	322.0 ± 202.8

NOTE—See description of each quantity in Table 3.

$1.7 \times 10^3 L_\odot$; see Molinari et al. 2008). However, the kinetic luminosity of the H I wind after inclination correction is $322.0 L_\odot$, i.e., $\sim 19\%$ of L_* . The ratio of $L_{\text{HI,wind}}/L_*$ after inclination correction is comparable to that in HH 7–11 (i.e., 20%) and in L1551 (i.e., 127%, see Giovanardi et al. 1992), while the ratio of $L_{\text{HI,wind}}/L_*$ before inclination correction is only $\sim 1\%$. This result implies that an inclination correction is necessary when we calculate the physical properties of the H I wind.

5. SUMMARY AND CONCLUSIONS

We obtained high-sensitivity H I spectra with an average rms noise of $\sim 7 \text{ mK @ } 0.1 \text{ km s}^{-1}$ toward the high-mass star-forming region G176.51+00.20 using FAST with a 19-beam tracking observational mode. We searched for H I wind in the central seven beams (i.e., Beams 1–7), but detected it only in Beam 1. The main results are as follows:

1. The abundance of H I in the H I wind is consistent with that of the HINSA (where the molecular column density is traced by ^{13}CO). This indicates that there probably exists an internal correlation between the H I wind and HINSA; such a correlation would enhance the argument of the association between the H I wind and the molecular outflows.

2. The H I wind is likely strong enough to drive the molecular outflows. This conclusion is not affected by the value of the inclination.
3. The mass, momentum, and kinetic energy of the H I wind and the associated mass-loss rate of the excitation star in G176.51+00.20, a high-mass star-forming region, are about one orders of magnitude larger than those in low-mass star-forming regions (i.e., HH 7–11 and L1551).

APPENDIX

A. MASS AND MOMENTUM OF THE H I WIND

A crude “triangular fit” was adopted to obtain the relationship between the brightness temperature and the radial velocity (e.g., [Lizano et al. 1988](#)) as

$$T_{\text{wind}}(v) = a + b \cdot v, \quad (\text{A1})$$

where a and b are constants with units of K and K (km s⁻¹)⁻¹, respectively. The result of the “triangular fit” is plotted as the red solid line in Figure 3(a). Considering that the H I wind may be contaminated or affected by the ambient environment, and manifesting as an asymmetry between the blue and red lobes, the blue and red lobes were fitted separately with the line center, $v_{\text{c,w}}$, as the velocity of HINSA (see [Li et al. 2022](#), see also Figure 2 and the red vertical line in Figure 3(a)).

T_{wind} can be used to calculate the column density of the H I wind as:

$$N_{\text{HI,wind}} = 1.82 \times 10^{18} \int T_{\text{wind}} dv, \quad (\text{A2})$$

where H I emission is assumed to be optically thin ([Dickey & Benson 1982](#); [Lizano et al. 1988](#); [Saha et al. 2018](#)).

The maximum velocity of the H I wind, $V_{\text{max,flow}}$, reads:

$$V_{\text{max,flow}} = -a/b, \quad (\text{A3})$$

and the mean velocity of the H I wind is $V_{\text{mean,flow}} = V_{\text{max,flow}}/3$ for the triangular profile. Considering that the beam size of FAST is 2'.9 and the distance to the H I wind is 1.8 kpc, the mass, $M_{\text{HI,wind}}$,

and momentum, $P_{\text{HI,wind}}$, of the H I wind without inclination correction are:

$$M_{\text{HI,wind}} = C_0 \int T_{\text{wind}} dv, \quad (\text{A4})$$

and

$$P_{\text{HI,wind}} = C_0 \int |v - v_{\text{c,w}}| T_{\text{wind}} dv, \quad (\text{A5})$$

respectively, where the constant C_0 is:

$$C_0 = 0.103 \text{ K}^{-1} M_{\odot} \text{ km}^{-1} \text{ s}, \quad (\text{A6})$$

where we assume that the hydrogen mass abundance is 0.74 (see [Garden et al. 1991](#)) and the H I wind emission is from a point source (e.g., [Lizano et al. 1988](#)). This is reasonable because the value of $V_{\text{max,flow}}$ is $120.6 \pm 16.3 \text{ km s}^{-1}$ (see [Lizano et al. 1988](#); [Frank et al. 2014](#), and references therein). The value of C_0 is larger than that in Equation (A6) by a factor of $2 \ln 2$ for an extended source with a uniform brightness temperature over the beam. The kinetic energy, $E_{\text{HI,wind}}$, of the H I wind is (see [Giovanardi et al. 1992](#)):

$$E_{\text{HI,wind}} = \frac{1}{2} M_{\text{HI,wind}} V_{\text{max,flow}}^2. \quad (\text{A7})$$

This work made use of the data from FAST. FAST is a Chinese national mega-science facility, operated by National Astronomical Observatories, Chinese Academy of Sciences. We would like to thank the anonymous referee for the helpful comments and suggestions that helped to improve the paper. This work was sponsored by the Natural Science Foundation of Jiangsu Province (grant No. BK20210999), the Entrepreneurship and Innovation Program of Jiangsu Province, NSFC grants Nos. 11933011 and 11873019, and the Key Laboratory for Radio Astronomy, Chinese Academy of Sciences.

Facility: FAST, PMO 13.7m

Software: Astropy ([Astropy Collaboration et al. 2013, 2018](#)), Matplotlib ([Hunter 2007](#)), Numpy ([Harris et al. 2020](#)), Pandas ([Wes McKinney 2010](#); [Reback et al. 2021](#)), Scipy ([Virtanen et al. 2020](#)), Emcee ([Foreman-Mackey et al. 2013](#))

REFERENCES

- Arce, H. G., Shepherd, D., Gueth, F., et al. 2007, in *Protostars and Planets V*, ed. B. Reipurth, D. Jewitt, & K. Keil, Tucson, AZ: Univ. Arizona Press, 245
- Astropy Collaboration, Robitaille, T. P., Tollerud, E. J., et al. 2013, *A&A*, 558, A33
- Astropy Collaboration, Price-Whelan, A. M., Sipőcz, B. M., et al. 2018, *AJ*, 156, 123
- Bally, J. 2016, *ARA&A*, 54, 491
- Chen, Y., Yao, Y., Yang, J., Zeng, Q., & Sato, S. 2003, *A&A*, 405, 655
- Dewangan, L. K. 2019, *ApJ*, 884, 84
- Dickey, J. M., & Benson, J. M. 1982, *AJ*, 87, 278
- Foreman-Mackey, D., Hogg, D. W., Lang, D., & Goodman, J. 2013, *PASP*, 125, 306
- Frank, A., Ray, T. P., Cabrit, S., et al. 2014, in *Protostars and Planets VI*, ed. H. Beuther, R. S. Klessen, C. P. Dullemond, & T. Henning, Tucson, AZ: Univ. Arizona Press, 451
- Garden, R. P., Hayashi, M., Gatley, I., Hasegawa, T., & Kaifu, N. 1991, *ApJ*, 374, 540
- Giovanardi, C., Lizano, S., Natta, A., Evans, Neal J., I., & Heiles, C. 1992, *ApJ*, 397, 214
- Harris, C. R., Millman, K. J., van der Walt, S. J., et al. 2020, *Nature*, 585, 357
- Herbig, G. H., & Jones, B. F. 1983, *AJ*, 88, 1040
- Hunter, J. D. 2007, *CSE*, 9, 90
- Jiang, P., Yue, Y., Gan, H., et al. 2019, *SCPMA*, 62, 959502
- Jiang, P., Tang, N.-Y., Hou, L.-G., et al. 2020, *RAA*, 20, 064
- Jiang, Z.-B., Chen, Z.-W., Wang, Y., et al. 2013, *RAA*, 13, 695
- Li, D., & Goldsmith, P. F. 2003, *ApJ*, 585, 823
- Li, D., Wang, P., Qian, L., et al. 2018, *IMMag*, 19, 112
- Li, Y., Xu, Y., Xu, J.-L., et al. 2022, *ApJL*, 933, L26
- Liu, D.-J., Xu, Y., Li, Y.-J., et al. 2022, arXiv e-prints, arXiv:2206.14544
- . 2021, *ApJS*, 253, 15
- Lizano, S., Heiles, C., Rodriguez, L. F., et al. 1988, *ApJ*, 328, 763
- McKee, C. F., & Ostriker, E. C. 2007, *ARA&A*, 45, 565
- Moffat, A. F. J., Fitzgerald, M. P., & Jackson, P. D. 1979, *A&AS*, 38, 197
- Molinari, S., Pezzuto, S., Cesaroni, R., et al. 2008, *A&A*, 481, 345
- Molinari, S., Testi, L., Rodríguez, L. F., & Zhang, Q. 2002, *ApJ*, 570, 758
- Nan, R. 2006, *ScChG*, 49, 129
- Nan, R., Li, D., Jin, C., et al. 2011, *IJMPD*, 20, 989
- Reback, J., jbrockmendel, McKinney, W., et al. 2021, pandas-dev/pandas: Pandas 1.3.4, v.v1.3.4, Zenodo, doi:10.5281/zenodo.5574486
- Saha, P., Roy, N., & Bhattacharya, M. 2018, *MNRAS*, 480, L126
- Shu, F. H., Adams, F. C., & Lizano, S. 1987, *ARA&A*, 25, 23

- Snell, R. L., Bally, J., Strom, S. E., & Strom, K. M. 1985, *ApJ*, 290, 587
- Snell, R. L., Huang, Y. L., Dickman, R. L., & Claussen, M. J. 1988, *ApJ*, 325, 853
- Snell, R. L., & Schloerb, F. P. 1985, *ApJ*, 295, 490
- Strom, K. M., Strom, S. E., Wolff, S. C., Morgan, J., & Wenz, M. 1986, *ApJS*, 62, 39
- Tan, J. C., Beltrán, M. T., Caselli, P., et al. 2014, in *Protostars and Planets VI*, ed. H. Beuther, R. S. Klessen, C. P. Dullemond, & T. Henning, Tucson, AZ: Univ. Arizona Press, 149
- Torrelles, J. M., Eiroa, C., Mauersberger, R., et al. 1992a, *ApJ*, 384, 528
- Torrelles, J. M., Gomez, J. F., Anglada, G., et al. 1992b, *ApJ*, 392, 616
- Virtanen, P., Gommers, R., Oliphant, T. E., et al. 2020, *Nature Methods*, 17, 261
- Wes McKinney. 2010, in *Proceedings of the 9th Python in Science Conference*, ed. Stéfan van der Walt & Jarrod Millman, Austin, Texas, 56 – 61
- Zhang, Q., Hunter, T. R., Brand, J., et al. 2005, *ApJ*, 625, 864